

# VelocityGAN: Subsurface Velocity Image Estimation Using Conditional Adversarial Networks

Zhongping Zhang

Los Alamos National Laboratory

zhongping@lanl.gov

Zheng Zhou

State University of New York at Buffalo

superfish2205@gmail.com

Yue Wu

University of California, Davis

yvwu@ucdavis.edu

Youzuo Lin

Los Alamos National Laboratory

ylin@lanl.gov

## Abstract

Acoustic- and elastic-waveform inversion is an important and widely used method to reconstruct subsurface velocity image. Waveform inversion is a typical non-linear and ill-posed inverse problem. Existing physics-driven computational methods for solving waveform inversion suffer from the cycle skipping and local minima issues, and not to mention solving waveform inversion is computationally expensive. In this paper, we developed a real-time data-driven technique, VelocityGAN, to accurately reconstruct subsurface velocities. Our VelocityGAN is an end-to-end framework which can generate high-quality velocity images directly from the raw seismic waveform data. A series of experiments are conducted on the synthetic seismic reflection data to evaluate the effectiveness and efficiency of VelocityGAN. We not only compare it with existing physics-driven approaches but also choose some deep learning frameworks as our data-driven baselines. The experiment results show that VelocityGAN outperforms the physics-driven waveform inversion methods and achieves the state-of-the-art performance among data-driven baselines.

## 1. Introduction

The reconstruction of the subsurface velocity image has been an important research topic in geoscience. In various applications such as oil & gas exploration, CO<sub>2</sub> sequestration, and geothermal exploration, the correct velocity image provides critical information in locating the resources and siting the drilling wells. Subsurface velocity inversion has attracted many attentions from both science and engineering domains. Overall, seismic velocity inversion can use either travel-time data or full waveform data. The travel time inversion is computationally effi-

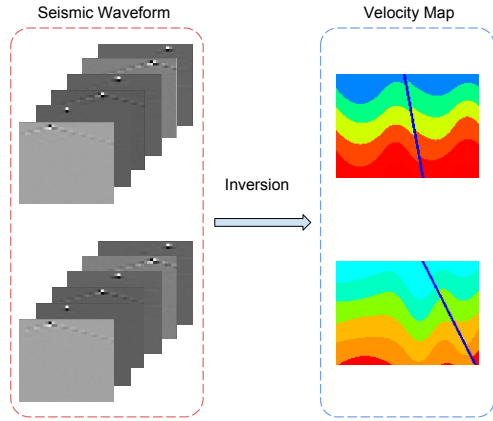


Figure 1. Examples of acoustic- and elastic-waveform inversion problem. Seismic waveforms are shown on the left-hand side. Velocity images are shown on the right-hand side. Though the seismic waveforms are almost the same to human eyes, their corresponding reconstructed velocity images are totally different.

cient, but it produces low-resolution velocity images [21]. The acoustic- and elastic-waveform inversion (AEWI) [38] progressively matches synthetic seismic waveform data to recorded data, and yields a velocity image that can be more accurate than the image obtained using travel time inversion. An intuitive illustration of seismic waveform inversion is provided in Figure 1. Even though AEWI is computationally more expensive than the travel time inversion, it becomes feasible in the recent years because of the increasing computing power. Most of the computational approaches to solve waveform inversion are physics-driven methods [37, 12, 5, 9]. For physics-driven methods, the reconstruction of velocity image is usually posed as an inverse problem, where the forward operator is provided as wave propagation. Because of the limited data coverage

and non-linearity of the wave equation, solving AEWI can be challenging [38]. One major issue is the cycle skipping, which results many local minima [13]. To alleviate the local minima problem, various computational techniques have been developed including using prior information-based approaches [23, 43, 25], multi-scale methods [3, 36], dynamic wrapping techniques [24, 28], and advanced regularization-based algorithms [4, 30, 9, 20]. The other major issue is the expensive computational cost [38]. The physics-driven techniques are iterative procedure. In each iteration, adjoint-state method is utilized to calculate a gradient map [27]. However, the computation of the gradient map requires the calculation of the forward wave-field and backward wave-field. With the gradient map obtained, nonlinear line search scheme is further required to obtain the optimal step sizes, which results in a few more forward modeling. The accumulated computation therefore becomes the bottleneck for efficient reconstruction of the velocity image.

To address the aforementioned issues of physics-driven methods, we develop a data-driven framework which takes the waveform data as the input and directly outputs its corresponding velocity image. Generative adversarial network (GAN) [8] has been proved to be successful in areas of photo inpainting [14], image denoising [40], super-resolution [18], image deblurring [17], and so forth. Motivated by these successes, we developed VelocityGAN to solve the AEWI problem. Unlike physics-driven methods, we interpret our task as an image-to-image problem. Specifically, VelocityGAN consists of two parts: generator and discriminator. Generator is an image-to-image structure which maps the raw seismic waveform data into velocity image. Discriminator is a convolutional neural network (CNN) designed to classify the real velocity image and fakes velocity image. Since VelocityGAN is a data-driven method, it is an end-to-end framework which can directly output the velocity map in real-time. Compared with the traditional AEWI problem, there are two improvements of VelocityGAN. Firstly, the parameters of VelocityGAN are trained on the whole dataset, therefore, local minima issue can be alleviated to some extent. Secondly, VelocityGAN is a real-time framework which can infer the unknown velocity image from seismic waveform data much more efficiently. We can analogize two image style transfer methods, [6] and [15], to better understand the above improvements. The main contributions of our work are:

- To the best of our knowledge, we are the first to apply conditional adversarial network on AEWI. VelocityGAN transfers the inverse process of physics-driven methods into an image mapping problem. As a result, it can alleviate the local minima and low computational efficiency issues.
- We propose a modified encoder-decoder structure which is

more suitable for AEWI. Besides, we combine mean absolute error (MAE) loss with mean square error (MSE) loss to further improve the quality of velocity images. Compared with the other deep learning baselines, our model is able to generate more accurate velocity images.

- We perform extensive experiments to demonstrate the effectiveness and efficiency of VelocityGAN, validating that VelocityGAN can generate higher quality velocity images in a much shorter time than physics-driven methods.

## 2. Related Work

### 2.1. AEWI

Acoustic- and elastic-waveform inversion (AEWI) is a powerful tool to estimate velocity in complex geological structures [12, 5, 10]. The input of AEWI can be either time-domain signals or frequency-domain signals [37, 12, 9]. Most existing papers [24, 4, 12, 9, 28, 35, 10, 36, 3, 25] consider AEWI as a numerical optimization process to inverse problems. Due to the non-linearity of the wave equation and limited data coverage, the local minima problem is unavoidable. A large number of efforts have been attempted to mitigate this problem. In [43], the authors incorporate the approximate location of a reservoir or a target monitoring region as the prior knowledge. Guitton *et al.* [10] apply the model-space preconditioning mechanism to obtain sharper velocity contrasts. Dynamic wrapping is another widely used technique in AEWI area. Qin *et al.* [28] propose a method combined with travel time picking using a dynamic wrapping technique. The output of their model can be used as the starting model for conventional AEWI frameworks. Recently, advanced regularization techniques [4, 12, 30, 1, 9, 20] become the most influential improvement for AEWI. Researchers use different kinds of regularization to improve their results. For example, L1-norm and L2-norm are presented in [1] and [12] respectively. In addition, some novel regularization techniques are also developed for solving AEWI, such as compressive sensing [19], Cauchy function regularization [9], and modified total-variation regularization [20]. More recently, with the successes of deep learning in image-to-image research [14, 45, 42], researchers begin to pay attention to the data-driven method. For example, [39] present a modified fully convolutional network (FCN) structure to address full-waveform inversion problem.

### 2.2. Generative Adversarial Networks

Generative Adversarial Networks (GANs) are firstly proposed by Goodfellow *et al.* [8]. In that paper, the authors present an adversarial mechanism which consists of a generator and a discriminator. The discriminator is designed to guide the generator to output more realistic images. Based on GANs, many popular and powerful frame-

works [26, 29, 14, 2, 11] are developed. Mirza *et al.* [26] introduce Conditional GANs which incorporate the classification label to generate specific category images. Except for the classification label, conditional GANs can also incorporate other information such as text [31], description data [7], image [14, 17] and so forth. When the input of conditional GANs is image, the generator is formulated as an image-to-image framework. Except for the wide applications of GANs, the stability of learning is another important research topic. For example, Arjovsky *et al.* [2] propose to replace Kullback-Leibler (KL) divergence with Wasserstein distance. The improvement can get rid of problems like mode collapse and provide meaningful learning curves. Starting with the success of Wasserstein GANs, Gulrajani *et al.* [11] introduce gradient penalty norm to take one step further.

In summary, existing frameworks of AEWI mostly focus on physics-driven methods. Motivated by the wide applications of conditional adversarial mechanism, we develop VelocityGAN to address the local minima and efficiency issues of AEWI. In VelocityGAN, a modified encoder-decoder, and a CNN are deployed as the generator and the discriminator.

### 3. The Model

We firstly present the governing wave equation in Section 3.1. In Section 3.2, we discuss our data-driven approach and the network structure of VelocityGAN. The loss function is discussed in Section 3.3.

#### 3.1. Acoustic- and Elastic-Waveform Inversion: Physics-Driven Approach

##### 3.1.1 Governing Physics - Wave Equation

Seismic waves are mechanical perturbations that travel in the Earth at a speed governed by the acoustic/elastic impedance of the medium in which they are traveling. In the time-domain, the acoustic-wave equation is given by

$$\left[ \frac{1}{K(\mathbf{r})} \frac{\partial^2}{\partial t^2} - \nabla \cdot \left( \frac{1}{\rho(\mathbf{r})} \nabla \right) \right] p(\mathbf{r}, t) = s(\mathbf{r}, t), \quad (1)$$

where  $\rho(\mathbf{r})$  is the density at spatial location  $\mathbf{r}$ ,  $K(\mathbf{r})$  is the bulk modulus,  $s(\mathbf{r}, t)$  is the source term,  $p(\mathbf{r}, t)$  is the pressure wavefield, and  $t$  represents time.

The elastic-wave equation is written as

$$\rho(\mathbf{r}) \ddot{u}(\mathbf{r}, t) - \nabla \cdot [C(\mathbf{r}) : \nabla u(\mathbf{r}, t)] = s(\mathbf{r}, t), \quad (2)$$

where  $C(\mathbf{r})$  is the elastic tensor, and  $u(\mathbf{r}, t)$  is the displacement wavefield.

The forward modeling problems in Eqs. (1) and (2) can be written as

$$P = f(\mathbf{m}), \quad (3)$$

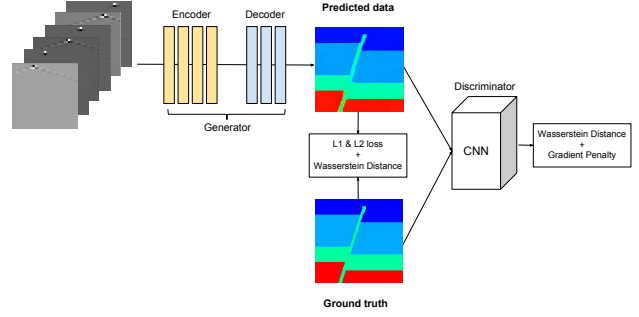


Figure 2. The overall architecture of VelocityGAN. We apply an encoder-decoder structure as the generator and a convolutional neural network as the discriminator.

where  $P$  is the pressure wavefield for the acoustic case or the displacement wavefields for the elastic case,  $f$  is the forward acoustic or elastic-wave modeling operator, and  $\mathbf{m}$  is the velocity model parameter vector, including the density and compressional- and shear-wave velocities. We use a time-domain stagger-grid finite-difference scheme to solve the acoustic- or elastic-wave equation. Throughout this paper, we consider only constant density acoustic or elastic media.

The inverse problem of Eq. (3) is usually posed as a minimization problem

$$E(\mathbf{m}) = \min_{\mathbf{m}} \left\{ \|\mathbf{d} - f(\mathbf{m})\|_2^2 + \lambda R(\mathbf{m}) \right\}, \quad (4)$$

where  $\mathbf{d}$  represents a recorded/field waveform dataset,  $f(\mathbf{m})$  is the corresponding forward modeling result,  $\|\mathbf{d} - f(\mathbf{m})\|_2^2$  is the data misfit,  $\|\cdot\|_2$  stands for the  $L_2$  norm,  $\lambda$  is a regularization parameter and  $R(\mathbf{m})$  is the regularization term which is often the  $L_2$  or  $L_1$  norm of  $\mathbf{m}$ .

##### 3.1.2 Data Generation

In practical applications, velocity models are estimated by physics-driven methods (usually an optimization algorithm). It can be unrealistic and expensive to obtain a large-scale dataset consisting of seismic waveform and velocity models. We therefore generate a dataset including velocity images and corresponding seismic waveform data generated using Eq. (2). The velocity images that we generated are varied with different tilting angles, layer thicknesses, and layer velocities etc. They can be a good representation of the real velocity images [22].

#### 3.2. VelocityGAN: Data-Driven Approach

Different from the physics-driven methods, VelocityGAN is a data-driven method. It transfers the minimization process into a mapping problem. The parameters of  $\mathbf{m}$  are

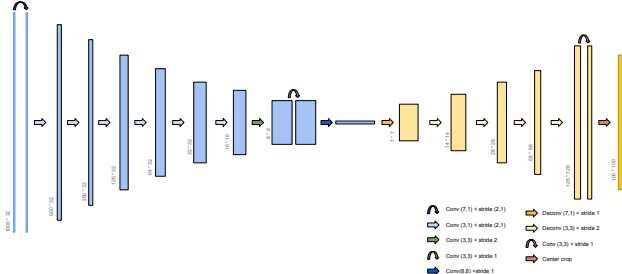


Figure 3. An illustration of the modified encoder-decoder structure.

directly learned from

$$\mathbf{m} = f^{-1}(\mathbf{d}), \quad (5)$$

where  $f^{-1}(\cdot)$  is the inverse operator of  $f(\cdot)$ . By VelocityGAN, only the parameters of  $f^{-1}(\cdot)$  need to be trained. We can directly map  $\mathbf{d}$  into its corresponding  $\mathbf{m}$  rather than solving for  $\mathbf{m}$  based upon each input seismic waveform and wave equation. The overall architecture of VelocityGAN is shown in Fig. 2. It consists of an image-to-image generator and a CNN discriminator. In the following sections, we discuss the structure of the generator and the discriminator respectively.

### 3.2.1 Generator

To better understand the network structure, we first recall the governing physics of our input and output data. In this paper, the input is the combination of the acoustic waves received by different receivers. Specifically, there are 3 source functions and 32 receivers, which correspond to  $s(\mathbf{r}, t)$  and  $P(\mathbf{r}, t)$  in Eq. (1) (or  $u(\mathbf{r}, t)$  in Eq. (2)), respectively. The source function may contain both P-wave and S-wave. Correspondingly, the seismic waveform data collected is a tensor with a dimension of  $32 \times 1000 \times 6$ , where the first dimension is 32 receivers, the second dimension of 1000 is the time sequence length of waveform trace, and the third dimension of 6 represents the total 2 channels of the 3 source functions. The output is a velocity image with dimension  $(m, n)$ , where the first dimension of  $m$  stands for depth and the second dimension of  $n$  stands for horizontal offset. The value of each pixel in the velocity image stands for the absolute velocity value at each location. The grid spacing between pixels is 5 meters. Therefore, the total size of velocity map is  $5m \times 5n$  meters.

As we discussed above, there is no specific spatial matchup between the input and output. So we do not penalize the mismatch between the input and output like [32]. Besides, since the height (1000) and width (32) of the input is unbalanced, we apply several convolutional layers with  $k \times 1$  kernels,  $k$  means the length of convolutional kernel

in height dimension. The particular structure of generator is shown in Figure 3. To extract the waveform features of each receiver, seven convolutional layers with  $k \times 1$  kernels are first deployed. Each convolutional layer is followed by a BatchNormalization layer and a LeakyReLU layer. After the dimension of height is reduced to 32,  $3 \times 3$  convolutional kernels with stride 2 are then added to encode the whole extracted features. In the last layer of encoder,  $8 \times 8$  convolutional kernels are used to eliminate the influence of spatial information. With regards to the decoder, it consists of a  $6 \times 6$  transposed convolution, five  $3 \times 3$  transposed convolutions, center cropping layer and a  $1 \times 1$  convolution. Transposed convolutions are applied to increase the height and width dimensions of image and decode the extracted features. Center cropping layer is used to crop the feature maps into a desired dimension.  $1 \times 1$  convolution is designed to map features into the same dimension with ground truth labels. To limit the value of output into a specific range, the  $1 \times 1$  convolution is followed by a Tanh Layer. We have also tried to replace the transposed convolution with upsampling layer like [32, 33]. It yields worse performance because the geologic fault of velocity map disappears.

### 3.2.2 Discriminator

Similar with [29], we adapt our discriminator from a CNN architecture. Particularly, it consists of five convolution blocks, a global average pooling layer, and fully connected layers. Each convolutional block involves a combination of Convolutional, BatchNormalization, LeakyReLU, and MaxPooling layer.

### 3.3 Loss Function

Wasserstein GAN (WGAN) with gradient penalty [11] has been proved to be robust of a wide variety of generator architectures. Considering the modified structure in our generator, we use Wasserstein loss with gradient penalty to distinguish the real image and the fake image. The loss function of discriminator is formulated as:

$$L_d = \mathbb{E}_{\tilde{x} \sim \mathbb{P}_g} D(\tilde{x}) - \mathbb{E}_{x \sim \mathbb{P}_r} D(x) + \lambda \mathbb{E}_{\hat{x} \sim \mathbb{P}_{\hat{x}}} [(\|\nabla_{\hat{x}} D(\hat{x})\|_2 - 1)^2], \quad (6)$$

where  $\mathbb{P}_g$  means the generator distribution,  $\mathbb{P}_r$  is the real data distribution, and  $\mathbb{P}_{\hat{x}}$  is random samples from both  $\mathbb{P}_g$  and  $\mathbb{P}_r$ .

For the generator, we want the predicted velocity map can not only fool the discriminator but also reveal the accurate information of geological structure. Therefore, the loss function is a combination of the adversarial loss and content loss. Consistent with Eq. (6), the adversarial loss is  $-\mathbb{E}_{\tilde{x} \sim \mathbb{P}_g} D(\tilde{x})$ . The content loss is set as a combination of mean absolute error (MAE) and mean square error (MSE).

In our experiments, we observe that MSE loss is good at capturing the geological faults while MAE loss performs better on revealing the geological interfaces. Therefore, the loss function of generator is formulated as:

$$L_g = -\mathbb{E}_{\tilde{x} \sim \mathbb{P}_g} D(\tilde{x}) + \frac{\lambda_1}{w \cdot h} \sum_{i=1}^w \sum_{j=1}^h |\tilde{v}(i, j) - v(i, j)| + \frac{\lambda_2}{w \cdot h} \sum_{i=1}^w \sum_{j=1}^h (\tilde{v}(i, j) - v(i, j))^2, \quad (7)$$

where  $w$  and  $h$  are the width and height of the velocity map respectively,  $v(\cdot)$  represents the real pixel value of the velocity map and  $\tilde{v}(\cdot)$  means the predicted pixel value.  $\lambda_1$  and  $\lambda_2$  are hyper-parameters to control the relative importance of the two loss term.

## 4. Experiments

We introduce the datasets and training details in Section 4.1. We discuss the experiment settings in Section 4.2. Following that, we compare and analyze the results of different methods.

### 4.1. Datasets and Training Details

#### 4.1.1 Datasets

Since there is no public dataset available for testing AEWI problem, we create two datasets by implementing our VelocityGAN, as discussed in Section 3.1. The first dataset contains 55,000 velocity images and their corresponding seismic waveform data. The velocity model is of 100 by 100 size with different tilting angle, layer thickness, and layer velocity. The geological layer interfaces and faults of this dataset are all straight. To avoid redundancy, we call this dataset “STData.” We also create a more challenging dataset compared with STData. It contains 50,000 velocity models with 150 by 100 dimension, along with their corresponding seismic waveform. Different from the STData, this dataset contains more geological layers in a velocity image. Furthermore, most geological layer interfaces are curved. We name this dataset as “CurvedData.” For both STData and CurvedData, 3 common-shot gather of synthetic seismic data with 32 receivers is posed at the top surface. We use a Ricker wavelet with a center frequency of 50 Hz as the source time function and a staggered-grid finite-difference scheme with a perfectly matched layered absorbing boundary condition to generate 2D synthetic seismic reflection data [34, 41]. The synthetic trace at each receiver is a collection of time-series data of length 1,000. Hence, the input size is (32, 1000, 6) where 1000 is the time sequence length, 32 is the number of receivers and 6 is the channel number.

#### 4.1.2 Training Details

For each dataset, we randomly select 5,000 velocity images as the testing set, 5,000 velocity images as the validation set to adjust the hyperparameters. We use the remaining images as the training set. The input of our model is normalized to range  $(-1 \sim 1)$ . Constrained by the memory of GPU, we set the size of mini-batch to 50. Following the optimization strategy of [2], we perform 5 gradient descent steps on the discriminator, and then perform one step on the generator. The learning rate of our Adam [16] optimizer is set to  $10^{-4}$  in the first 120 epochs. After the first 120 epochs, we linearly decay the learning rate to 0 over the next 170 epochs. For discriminator loss (Eq. (6)), we choose  $\lambda$  as 10. For generator loss (Eq. (7)),  $\lambda_1$  and  $\lambda_2$  are set to 0 and 100 in STData, 50 and 100 in CurvedData. All of our models are implemented on a single GTX 1080-Ti using PyTorch framework. Approximately, the training process of VelocityGAN takes two days.

### 4.2. Experiment Settings

Velocity image generation experiments are conducted to evaluate the effectiveness of our VelocityGAN. We choose the following algorithms from both physics-driven and data-driven methods as our baselines:

- AEWI-Pre [44]: A wave-energy-based precondition method is applied to reduce the artifacts in the gradients caused by the geometrical spreading and defocusing effects.
- AEWI-MTV [20]: A modified total-variation regularization (MTV) is used as a regularization term in AEWI optimization process. MTV is designed to preserve sharp interfaces in piecewise constant structures.
- FCN [33]: We adjust the dimension of several convolutions in FCN to make it work on our project.
- U-Net [32]: Based on a typical encoder-decoder structure, U-Net adds skip connections between mirrored layers in the encoder and decoder stacks.
- modifiedFCN [39]: A modified FCN framework for full waveform inversion (FWI) problem.

Specifically, AEWI-Pre [44] and AEWI-MTV [20] are physics-driven methods. FCN [33], U-Net [32] and modifiedFCN [39] are selected as the data-driven frameworks for solving AEWI problem. For quantitative experiments, we adopt the MAE and MSE loss to evaluate the accuracy of geological layer information. For qualitative experiments, we present several velocity image samples and vertical velocity profiles to provide an intuitive comparison. It is worthwhile to mention that in both STData and

Table 1. Comparison of MAE loss, MSE loss, and implementation time on STData. The value of MSE and MAE is on the basis of  $10^{-2}$

	MAE	MSE	time (ms)
AEWI-Pre [44]	11.61	3.58	16 hours
AEWI-MTV [20]	7.08	2.00	16 hours
FCN [33]	5.11	1.53	5.72
U-Net [32]	5.27	1.41	2.71
modifiedFCN [39]	6.34	0.97	4.40
Generator (ours)	2.29	0.31	2.92
VelocityGAN (ours)	1.99	0.21	3.04

Table 2. Comparison of MAE loss and MSE loss on CurvedData. The value of MSE and MAE is on the basis of  $10^{-2}$

	MAE	MSE
AEWI-Pre [44]	13.45	4.96
AEWI-MTV [20]	11.34	4.25
Generator + MAE	22.92	10.32
Generator + MSE	26.55	12.11
Generator	19.91	8.84
VelocityGAN + MAE	19.31	7.67
VelocityGAN + MSE	17.31	7.17
VelocityGAN	7.38	2.44

CurvedData, we include a small geologic fault in the velocity model. Geologic faults play an important role in siting the wells in subsurface applications because of its high permeability property. However, it can be technical challenging to image a geologic fault zone due to the limited imaging resolution and data coverage. We will compare our method to others not only in the overall reconstruction quality, but also in the local region such as fault zone. Besides, we also compare the implementation time of different approaches.

### 4.3. STData

#### 4.3.1 Quantitative Results

In this section, we demonstrate the quantitative results of STData in Table 1. Generator is the modified encoder-decoder structure we discussed in Section 3.2. As the table shows, all data-driven methods achieve better MAE and MSE results than physics-driven methods. Among the data-driven methods, the proposed generator has already outperformed the other baselines. To further improve the model, we apply the adversarial training strategy on the generator and construct our VelocityGAN. The results demonstrate that VelocityGAN further improves the results based on the Generator model.

Time comparison reflects the efficiency of these models. Obviously, the implementation time of physics-driven methods is much longer than data-driven methods. Approximately, physics-driven methods take 16 hours to pro-

duce only one velocity image, which means it is impractical to apply physics-driven methods for real-time inversion of seismic data. As a result, we randomly choose 5 samples and calculate their average loss. In contrast, data-driven methods take only a few milliseconds. The implementation time results prove that the data-driven methods are much more efficient than physics-driven approaches. They can achieve real-time image reconstruction from seismic waveform data.

#### 4.3.2 Qualitative Results

To compare the visual appearance of our models, we randomly select five groups of velocity images and illustrate them in Fig. 4, where the left most column is the ground true. As shown in Fig. 4, the geological layer interfaces and faults constructed by physics-driven methods are blurry and inaccurate. Some layer interfaces and geologic fault zone in the deep region even disappear in those results obtained using physics-driven methods. For data-driven methods, most layer interfaces are well constructed. However, in the results of U-Net, the geological faults cannot be revealed. We believe this as the influence of upsampling layers because the boundary error of fault information will be accumulated by upsampling layers. The visual appearance of modifiedFCN and FCN achieve similar results. The main issue of these two methods is that the fault and layer interface are blurry to some extent. Comparatively, VelocityGAN can generate high-quality images mostly correspond to the ground truth images. Both the fault and layer interface are relatively clear and sharp.

### 4.4. CurvedData

In the real world, influenced by crustal movements, the geological layers are usually not straight as shown in the STData. To address the curved layer estimation, we create a more challenging dataset – CurvedData. In STData, MAE loss is good enough to achieve satisfying results. However, in CurvedData, geological faults will disappear with the constraint of MAE loss. MSE loss is good at revealing geological faults but does not perform well on reconstructing the layer interfaces. Therefore, we use a combination of MAE and MSE loss to generate more accurate velocity images. In our quantitative experiments, we not only compare VelocityGAN with physics-driven models but also do ablation study on the combination of loss.

#### 4.4.1 Quantitative Results

Table 2 shows the quantitative results of MAE loss and MSE loss on CurvedData. We can see that our proposed models still outperform the other baselines. Besides, a model with a combination of MAE and MSE can always achieve better

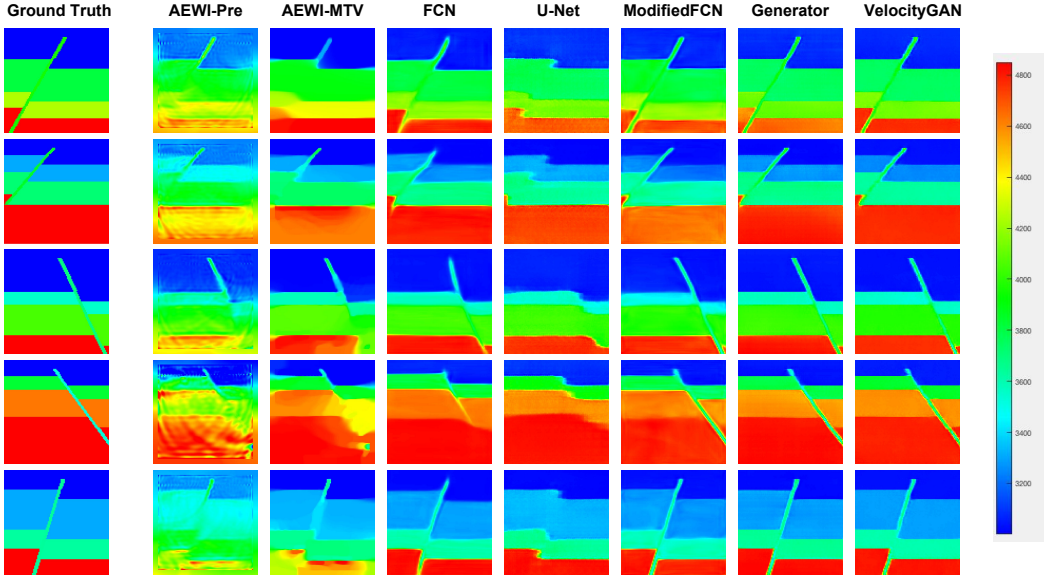


Figure 4. Examples of different methods on STData. The images from left most columns to right are ground truth, reconstruction results using AEWI-Pre [44], AEWI-MTV [20], FCN [33], U-Net [32], modifiedFCN [39], Generator (ours), and VelocityGAN (ours). Our VelocityGAN yields the most accurate reconstructed velocity images comparing to both physics-driven and data-driven approaches.

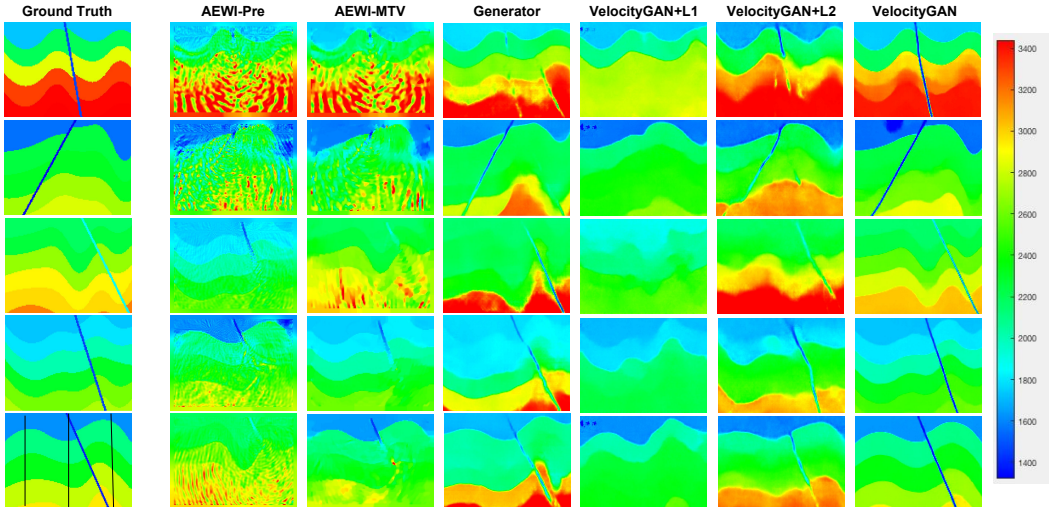


Figure 5. Examples of different methods on CurvedData. The images from left most columns to right are ground truth, reconstruction results using AEWI-Pre [44], AEWI-MTV [20], Generator, VelocityGAN+L1, VelocityGAN+L2, and VelocityGAN. Our VelocityGAN yields the most accurate reconstructed velocity images comparing to both physics-driven and data-driven approaches.

prediction results than a single loss. The quantitative experiments on STData and CurvedData validate that the generator structure, adversarial training strategy, and the combination of losses are all useful improvements and can boost the reconstructed results.

#### 4.4.2 Qualitative Results

We illustrate reconstructions of velocity images using different baseline methods in Figure 5. Consistent with our discussion on loss function, VelocityGAN with MAE loss is good at handling with the boundary of geological layers, however, it ignores the geological faults and high-velocity

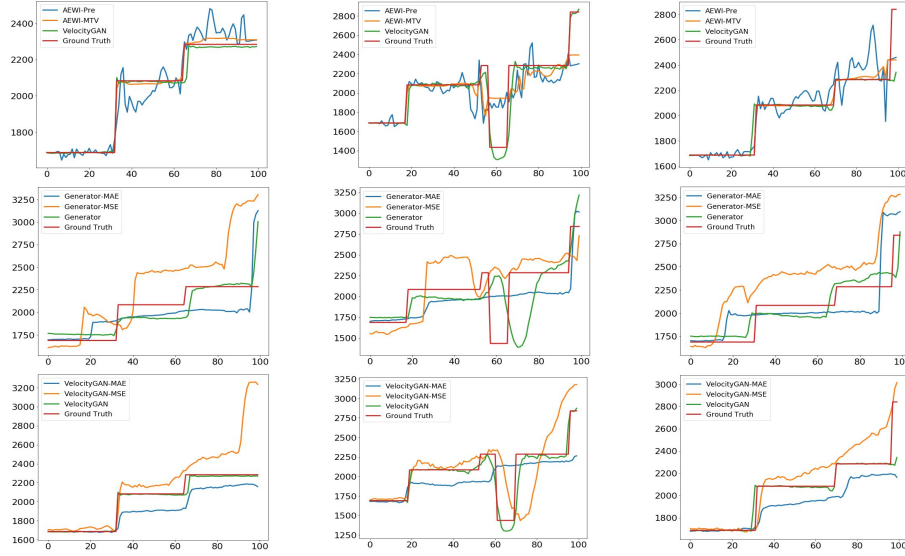


Figure 6. Vertical velocity profiles of different positions. From left to right, the positions are 30, 75, 110, respectively. To illustrate the profile locations, 3 vertical lines are plotted in Figure 5. We compare VelocityGAN with physics-driven methods in the first row, compare Generator with different loss functions in the second row, and compare VelocityGAN with different loss functions in the third row.

areas. VelocityGAN with MSE loss can generate geological faults but the boundary of geological layers are fuzzy. VelocityGAN with a combination of MAE and MSE can achieve a better tradeoff between the quality of geological layer interfaces and faults. Besides, physics-driven methods does not perform as well as the quantitative results shows. There are many oscillations in deep region and high-velocity areas, which can be observed in the first three rows as shown in Fig. 5. This is because we only calculate the average loss of five selected images for physics-driven methods, the quantitative results can be mis-leading.

To visualize the reconstruction accuracy, we also provide a vertical velocity profile of each reconstructed image along with the ground truth in Fig. 6. The vertical velocity profile means that we randomly select a horizontal position on a velocity image, and then plot the vertical velocities along this horizon position. We compare our results to those obtained using physics-driven methods as shown in the first row in Fig. 6. We observe that the vertical velocity profile of physics-driven methods oscillates significantly, although the overall trend of physics-driven methods is correct. In the second and third row in Fig. 6, we observe that frameworks with MAE loss (Generator-MAE and VelocityGAN-MAE) always yield much lower velocity values in high-velocity regions. In contrast, frameworks with MSE loss (Generator-MSE, VelocityGAN-MSE) tend to yield higher values in high-velocity areas. In addition, frameworks with single loss sometimes completely miss the geological fault zones. A combination of loss alleviates those issues. For example, in the third row and second column, both VelocityGAN-

MAE and Velocity-MSE fail to reconstruct the geologic fault zone between position 60 and 70. In contrast, VelocityGAN with a combination of MAE and MSE produce a correct reconstruction of the fault zone. According to these profiles comparison, we show that our VelocityGAN yields more accurate reconstruction of velocity image in obtaining both global and location geologic features.

## 5. Conclusion

We develop VelocityGAN, a data-driven method, to solve the acoustic- and elastic-waveform inversion problem. We design a modified encoder-decoder structure as the core block of image-to-image target. Based on the encoder-decoder structure, conditional adversarial training strategy with improved loss function are applied to further boost the reconstruction of velocity images. Compare with physics-driven methods, VelocityGAN is a more promising tool for subsurface velocity estimation, because it can alleviate the local minima and expensive computational cost issues. We provide extensive experiments to demonstrate the effectiveness and efficiency of our VelocityGAN from various aspects. The results substantiate that our model outperforms both the physics-driven methods and the selected deep learning baselines.

## 6. ACKNOWLEDGMENTS

This work was supported by the Center for Space and Earth Science (CSES) at Los Alamos National Laboratory (LANL).

## References

[1] A. Y. Anagaw and M. D. Sacchi. Full waveform inversion with total variation regularization. In *Recovery-CSPG CSEG CWLS Convention*, 2011.

[2] M. Arjovsky, S. Chintala, and L. Bottou. Wasserstein gan. *arXiv preprint arXiv:1701.07875*, 2017.

[3] C. Bunks, F. M. Saleck, S. Zaleski, and G. Chavent. Multi-scale seismic waveform inversion. *Geophysics*, 60(5):1457–1473, 1995.

[4] C. Burstedde and O. Ghattas. Algorithmic strategies for full waveform inversion: 1d experiments. *Geophysics*, 74(6):WCC37–WCC46, 2009.

[5] A. Fichtner. *Full seismic waveform modelling and inversion*. Springer Science & Business Media, 2010.

[6] L. A. Gatys, A. S. Ecker, and M. Bethge. A neural algorithm of artistic style. *arXiv preprint arXiv:1508.06576*, 2015.

[7] J. Gauthier. Conditional generative adversarial nets for convolutional face generation. *Class Project for Stanford CS231N: Convolutional Neural Networks for Visual Recognition, Winter semester, 2014*(5):2, 2014.

[8] I. Goodfellow, J. Pouget-Abadie, M. Mirza, B. Xu, D. Warde-Farley, S. Ozair, A. Courville, and Y. Bengio. Generative adversarial nets. In *Advances in neural information processing systems*, pages 2672–2680, 2014.

[9] A. Guitton. Blocky regularization schemes for full-waveform inversion. *Geophysical Prospecting*, 60(5):870–884, 2012.

[10] A. Guitton, G. Ayeni, and E. Díaz. Constrained full-waveform inversion by model reparameterization geologically constrained fwi. *Geophysics*, 77(2):R117–R127, 2012.

[11] I. Gulrajani, F. Ahmed, M. Arjovsky, V. Dumoulin, and A. C. Courville. Improved training of wasserstein gans. In *Advances in Neural Information Processing Systems*, pages 5767–5777, 2017.

[12] W. Hu, A. Abubakar, and T. M. Habashy. Simultaneous multifrequency inversion of full-waveform seismic data. *Geophysics*, 74(2):R1–R14, 2009.

[13] W. Hu, J. Chen, J. Liu, and A. Abubakar. Retrieving low wavenumber information in fwi: An overview of the cycle-skipping phenomenon and solutions. *IEEE Signal Processing Magazine*, 35:132–141, 2018.

[14] P. Isola, J.-Y. Zhu, T. Zhou, and A. A. Efros. Image-to-image translation with conditional adversarial networks. *arXiv preprint*, 2017.

[15] J. Johnson, A. Alahi, and L. Fei-Fei. Perceptual losses for real-time style transfer and super-resolution. In *European Conference on Computer Vision*, pages 694–711. Springer, 2016.

[16] D. P. Kingma and J. Ba. Adam: A method for stochastic optimization. *arXiv preprint arXiv:1412.6980*, 2014.

[17] O. Kupyn, V. Budzan, M. Mykhailych, D. Mishkin, and J. Matas. Deblurgan: Blind motion deblurring using conditional adversarial networks. *arXiv preprint arXiv:1711.07064*, 2017.

[18] C. Ledig, L. Theis, F. Huszár, J. Caballero, A. Cunningham, A. Acosta, A. P. Aitken, A. Tejani, J. Totz, Z. Wang, et al. Photo-realistic single image super-resolution using a generative adversarial network. In *CVPR*, volume 2, page 4, 2017.

[19] X. Li, A. Y. Aravkin, T. van Leeuwen, and F. J. Herrmann. Fast randomized full-waveform inversion with compressive sensing. *Geophysics*, 77(3):A13–A17, 2012.

[20] Y. Lin and L. Huang. Acoustic-and elastic-waveform inversion using a modified total-variation regularization scheme. *Geophysical Journal International*, 200(1):489–502, 2014.

[21] Y. Lin, E. Syracuse, M. Maceira, H. Zhang, and C. Laramat. Double-difference traveltime tomography with edge-preserving regularization and a priori interfaces. *Geophysical Journal International*, 201(2):574–594, 2015.

[22] Y. Lin, S. Wang, J. Thiagarajan, G. Guthrie, and D. Coblenz. Efficient data-driven geologic feature characterization from pre-stack seismic measurements using randomized machine-learning algorithm. *Geophysical Journal International*, 2018 (accepted).

[23] Y. Ma and D. Hale. Quasi-newton full-waveform inversion with a projected hessian matrix. *Geophysics*, 77(5):R207–R216, 2012.

[24] Y. Ma and D. Hale. Wave-equation reflection traveltime inversion with dynamic warping and full-waveform inversion with dynamic warping. *Geophysics*, 78(6):R223–R233, 2013.

[25] Y. Ma, D. Hale, B. Gong, and Z. Meng. Image-guided sparse-model full waveform inversion. *Geophysics*, 77(4):R189–R198, 2012.

[26] M. Mirza and S. Osindero. Conditional generative adversarial nets. *arXiv preprint arXiv:1411.1784*, 2014.

[27] R. E. Plessix. A review of the adjoint-state method for computing the gradient of a functional with geophysical applications. *Geophysical Journal International*, 167:495–503, 2006.

[28] F. Qin, T. W. Fei, and Y. Luo. Velocity model building from waveform tomography of band limited reflection seismic data. In *SEG Technical Program Expanded Abstracts 2013*, pages 866–870. Society of Exploration Geophysicists, 2013.

[29] A. Radford, L. Metz, and S. Chintala. Unsupervised representation learning with deep convolutional generative adversarial networks. *arXiv preprint arXiv:1511.06434*, 2015.

[30] A. C. Ramírez and W. R. Lewis. Regularization and full-waveform inversion: A two-step approach. In *SEG Technical Program Expanded Abstracts 2010*, pages 2773–2778. Society of Exploration Geophysicists, 2010.

[31] S. Reed, Z. Akata, X. Yan, L. Logeswaran, B. Schiele, and H. Lee. Generative adversarial text to image synthesis. *arXiv preprint arXiv:1605.05396*, 2016.

[32] O. Ronneberger, P. Fischer, and T. Brox. U-net: Convolutional networks for biomedical image segmentation. In *International Conference on Medical image computing and computer-assisted intervention*, pages 234–241. Springer, 2015.

[33] E. Shelhamer, J. Long, and T. Darrell. Fully convolutional networks for semantic segmentation. *arXiv preprint arXiv:1605.06211*, 2016.

- [34] S. Tan and L. Huang. An efficient finite-difference method with high-order accuracy in both time and space domains for modelling scalar-wave propagation. *Geophysical Journal International*, 197(2):1250–1267, 2014.
- [35] Y. Tang and S. Lee. Preconditioning full waveform inversion with phase-encoded hessian. In *SEG Technical Program Expanded Abstracts 2010*, pages 1034–1038. Society of Exploration Geophysicists, 2010.
- [36] K. T. Tran, M. McVay, M. Faraone, and D. Horhota. Sink-hole detection using 2d full seismic waveform tomography sinkhole detection by fwi. *Geophysics*, 78(5):R175–R183, 2013.
- [37] D. Vigh and E. W. Starr. Comparisons for waveform inversion, time domain or frequency domain? In *SEG Technical Program Expanded Abstracts 2008*, pages 1890–1894. Society of Exploration Geophysicists, 2008.
- [38] J. Virieux and S. Operto. An overview of full-waveform inversion in exploration geophysics. *Geophysics*, 74(6):WCC1–WCC26, 2009.
- [39] W. Wang, F. Yang, and J. Ma. Velocity model building with a modified fully convolutional network. In *SEG Technical Program Expanded Abstracts 2018*, pages 2086–2090. Society of Exploration Geophysicists, 2018.
- [40] Q. Yang, P. Yan, Y. Zhang, H. Yu, Y. Shi, X. Mou, M. K. Kalra, Y. Zhang, L. Sun, and G. Wang. Low dose ct image denoising using a generative adversarial network with wasserstein distance and perceptual loss. *IEEE transactions on medical imaging*, 2018.
- [41] W. Zhang and Y. Shen. Unsplit complex frequency shifted PML implementation using auxiliary differential equation for seismic wave modeling. *Geophysics*, 75:T141–T154, 2010.
- [42] Z. Zhang, T. Chen, Z. Zhou, J. Li, and J. Luo. How to become instagram famous: Post popularity prediction with dual-attention. In *2018 IEEE International Conference on Big Data (Big Data)*, pages 2383–2392. IEEE, 2018.
- [43] Z. Zhang and L. Huang. Double-difference elastic-waveform inversion with prior information for time-lapse monitoring. *Geophysics*, 78(6):R259–R273, 2013.
- [44] Z. Zhang, L. Huang, and Y. Lin. A wave-energy-based precondition approach to full-waveform inversion in the time domain. In *SEG Technical Program Expanded Abstracts 2012*, pages 1–5. Society of Exploration Geophysicists, 2012.
- [45] Z. Zhang, Y. Zhang, Z. Zhou, and J. Luo. Boundary-based image forgery detection by fast shallow cnn. *arXiv preprint arXiv:1801.06732*, 2018.